Intricate multiple scattering features of artificial facilities in X-Band SAR images

Sijie Ma[1], Tao Li[1], Yan Liu[2], Jie Liu[1]

[1] GNSS Research Center of Wuhan University, Wuhan 430070, Hubei, China
[2] State Key Laboratory of Power Grid Environmental Protection, China Electric Power Research Institute, China

Keywords: SAR, Artificial facilities, Multiple scattering, LiDAR cloud points, Scattering point path tracking model.

Abstract

Due to the intricate distortion and reflection geometry of the SAR signal, it is typically difficult to determine the multiple scattering of large artificial objects in SAR images. This work presents a scattering point path tracking model that utilizes the real three-dimensional dimensions of targets, based on the geometric optics method. Three different artificial structures, including light poles, cable stayed bridges, and power transmission lines, are carefully analysed in time-series SAR images with their simulated multiple scattering results. The results demonstrate that the routes determined by the model are consistent with the multiple scattering features on SAR images. Moreover, the time-series data demonstrate that ripples in the water's surface have a significant impact on the multi-scattering features of power lines and bridges. The double scattering features of the light pole provides a novel approach to the process of permanent scatterers (PS) in urban areas. The instances presented in this study demonstrate the effectiveness of the scattering point path tracking model in identifying the various artificial facility targets on different reflective surfaces. It will be a useful tool for deciphering the multiple scattering of large artificial structures when their 3D model is known.

1. Introduction

A SAR image contains the radar backscatter intensity, the phase of the backscatter signal, and the distance from the sensor to the target (Matikainen et al., 2016). Radar signals can generate multiple scattering effects in the angular structure of artificial facilities, especially under the angular structures with smooth ground and water surfaces. Therefore, artificial facilities contain abundant scattering features in SAR images. With the improvement of SAR satellite resolution and revisit period, SAR images are ready to contain a large amount of detailed information in periodic order (Auer et al., 2010). However, the interpretation of high-resolution SAR images is difficult especially in urban area for the different geometric configurations of artificial facilities and the overlap of the multi-scattering. The multiple scattering effects of Egyptian pyramids (Bamler and Eineder, 2008) and bridges are the most typical, which are generated by smooth ground or water surfaces (Kim and Lee, 2022). Specifically, some large artificial metal facilities also exhibit multiple scattering effects of SAR signals inside their structure, such as large oil storage tanks (Zhang and Liu, 2020), the Eiffel Tower, etc. (Auer et al., 2010). It should be noted that the shape of the targets on SAR images are different from its real shape, making it difficult to distinguish, especially the multiple scattering features.

Thus, accurately understanding these multiple scattering features can help in better extracting and detecting ground targets and separating them (Zeng et al., 2017). Bridges are typical cases of multi-scattering, exhibiting linear scattering features with their own shapes. Jong-Sen Lee et al. derived the multi-scattering model for bridges (Lee et al., 2006). They took the vertical point as the reference point and calculated the range difference in multi-scattering without the liDAR points for further verification. Soergel et al. extracted the single, double, and triple features of bridges from SAR images in 2007 (Soergel et al., 2007). Kim et al. used the multiple scattering features of bridges from CSK data for accurate water level measurement in 2022 (Kim and Lee, 2022).

Compared to artificial facilities such as bridges with typical scattering structures, power lines cannot maintain their consistent shape characteristics in SAR images. Many scholars have studied the radar phenomenology of power lines in millimeter-wave radar system (Sarabandi et al., 1994; Sarabandi and Moonsoo Park, 2003, 1999). Liu et al. firstly discovered that power lines exhibit speckled scattering characteristics in spaceborne SAR images in 2012, suggesting that this scattering pattern is caused by the signal direct bounce (Yan et al., 2012). Li Sha et al. found that the strict conditions for the angle between the lines and the flight direction of the radar satellite (Li Sha et al., 2014; Shi et al., 2021). Chen Zhiguo et al. revealed that the phase features of the line scatters fluctuated irregularly (Chen et al., 2016). And power lines’ scattering features in multi-bands have been evaluated for monitoring purposes utilizing spaceborne SAR images (Shi et al., 2020; Willetts et al., 2018).

Therefore, the paper proposes a scattering point path tracking model to further interpret the multi-scattering features. The model can calculate any artificial facility with its liDAR points data, which enables further accurate simulation and interpretation of artificial facility targets. Three typical artificial facility targets have been selected based on actual three-dimensional liDAR point data from 102 scenes of TSX data in the Badong area of Hubei, China. The results show that the simulation results

* Corresponding author: Tao Li , e-mail: TaoLi@whu.edu.cn

calculated by the model are consistent with the scattering features on real SAR images. Additionally, we contrast how different water surface fluctuation levels affect the imaging of multiple scattering features. The outcomes offer a benchmark for the actual target condition of SAR image characteristics, as well as offering a new and effective technique for monitoring large artificial facility targets.

2. Method and Data

2.1 Scattering Point Path Tracking Model

The multiple scattering of artificial facility targets is usually caused by the angular structure composed of the side and bottom surfaces of the buildings. And it is affected by factors such as the incident angle of SAR satellites, the effective sizes in scattering. Therefore, in this paper, we assume that the artificial facility target consists of the numerous point targets, which all exist uniform backscattering of radar signals. Taken a point as N_i from these sequential points shown in Figure 1a, red arrows indicate the single bounce, which means radar signals directly return once they reach the target. Under this situation, the target point N_i is compressed to a smaller pixel-unit point on SAR image according to the Range Doppler Algorithm (RDA). The pixel-unit point on SAR image called as N'_i corresponding to N_i in the real world.

As for the double bounce shown as the green arrows in Figure 1a, the SAR signal passes through the reflection surface P and then undergoes specular reflection to N_i and finally returns to the SAR sensors. Under the double bounce, the scattering path extends and the N_i would form another scattering point on SAR image which named as N''_i in Figure 1b. The double scattering usually originates from the sides of the facilities, which forms effective scattering surfaces like cylindrical surfaces and side elevation. It is difficult to confirm the specific coordinates of vertical point N_{i_g}, so N'_i was adopted as starting point to compare the range difference in single, double and triple bounce. Equation 1 shows the increment of the double scattering in range direction:

$$S_{N'_iN''_i} = \frac{(R1 + R2)}{2} \tag{1}$$

Where $S_{N'_iN''_i}$ is the total length of the double scattering path extension in meters, $R1$ and $R2$ are the parts of the double scattering path extension of the SAR signal, and the specific expressions for $R1$ and $R2$ are as followings:

$$\begin{aligned} R1 &= R2 * \cos 2\eta \\ R2 &= \frac{\Delta h_{N_i}}{\cos \eta} \end{aligned} \tag{2}$$

Where Δh_{N_i} is the elevation difference from the target point N_i and water surface and η is the local incident angle. Further, the number of pixels between N'_i and the double scattering point N''_i in the SAR image range direction can be obtained, which is calculated as Equation 3:

$$P_{N'_iN''_i} = \Delta h_{N_i} * \frac{\cos \eta}{D_r} \tag{3}$$

Where D_r is the resolution in range direction of the SAR data and Δh_{N_i}, η, D_r are all known observations for the target observation points.

The purple arrows in Figure 1a indicate that the radar signals pass through the reflection surface and specular reflection occurs to N_i and then back to SAR sensors in the original way. This progress is called triple bounce, which usually comes from the bottom of the building (such as the bottom of the ball, the bottom of the bridge), or structure with dihedral angle structure (side of the downward dihedral angle), as well as the bottom of the cylinder (such as power lines) and so on. The signal is further extended by the three scattering paths, N_i will form another target point N'''_i on the SAR image as shown by the purple point in Figure 1b. Similarly, this paper takes the target point N'_i as the reference and then deduces the increment of the N'''_i and N'_i as shown in Equation 4:

$$S_{N'_iN'''_i} = R1 + R2 \tag{4}$$

Where $S_{N'_iN'''_i}$ is the total length of the triple scattering path extension in meters. Further, the number of pixels between N'_i and the triple scattering point N'''_i in range direction can be obtained as Equation 5:

$$P_{N'_iN'''_i} = 2 * \Delta h_{N_i} * \frac{\cos \eta}{D_r} \tag{5}$$

It is worth noting that if the vertical point N_{i_g} directly imaged in the SAR image schematised N'_{i_g} in Figure 1b, the increment of the N'_i and N'_{i_g} is calculated as following:

$$P_{N'_iN'_{i_g}} = \Delta h_{N_i} * \frac{\cos \eta}{D_r} \tag{6}$$

Combined Equation 1~6, the target point N_i would form the single, double, triple scattering spots on SAR images. While the point N'_{i_g} corresponding to the reflective surface pendant point of N_i is coincidence with N''_i. And the point N''_i is the bisecting point between the single scattering spot N'_i and the triple scattering spot N'''_i.

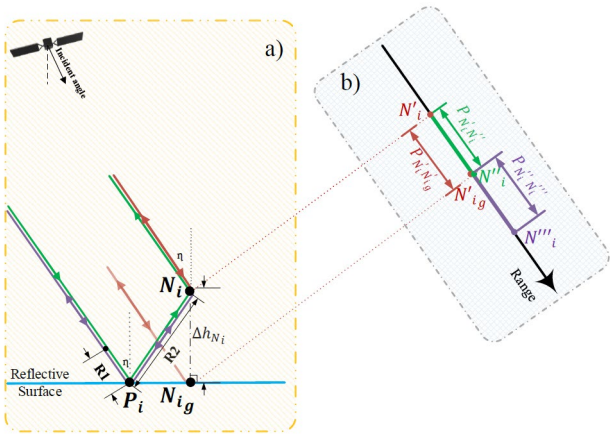

Figure 1. Scattering Point Path Tracing Model. (a) represents the multiple scattering path of the SAR signal in real space. (b) represents the SAR imaging location in range direction.

The radar signals path will increase under the multi-scattering, and N_i will form the N'_i, N''_i, N'''_i in range direction sequentially according to Equation 3-5.

Therefore, based on the different multi-scattering spots' range locations generated by the same target N_i, it is possible to carry out the prejudgement of the structure in multi-scattering, but it is

not able to carry out the accurate and detail interpretation of the structure. While based on the multi-scattering path tracking model, simulation results of multiple scattering considering the structure can be obtained shown as Figure 2.

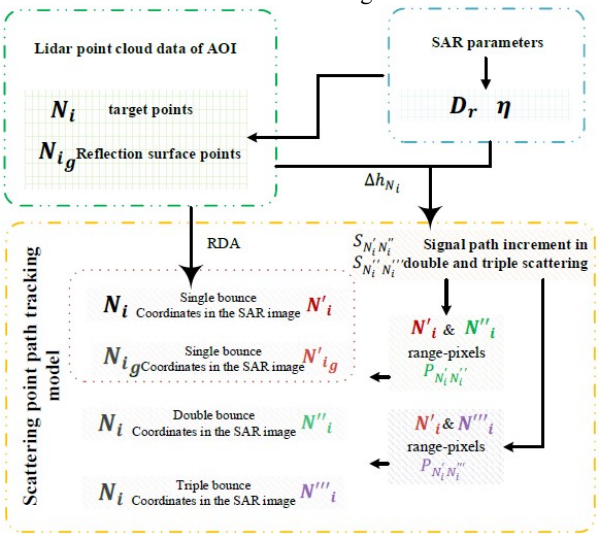

Figure 2. Simulation process for scattering point path tracking model.

2.2 Experimental Data

In this paper, typical artificial facilities are selected in three areas in Badong region shown as Figure 3a to simulate and verify the scattering point tracking model considering the scattering target structure.

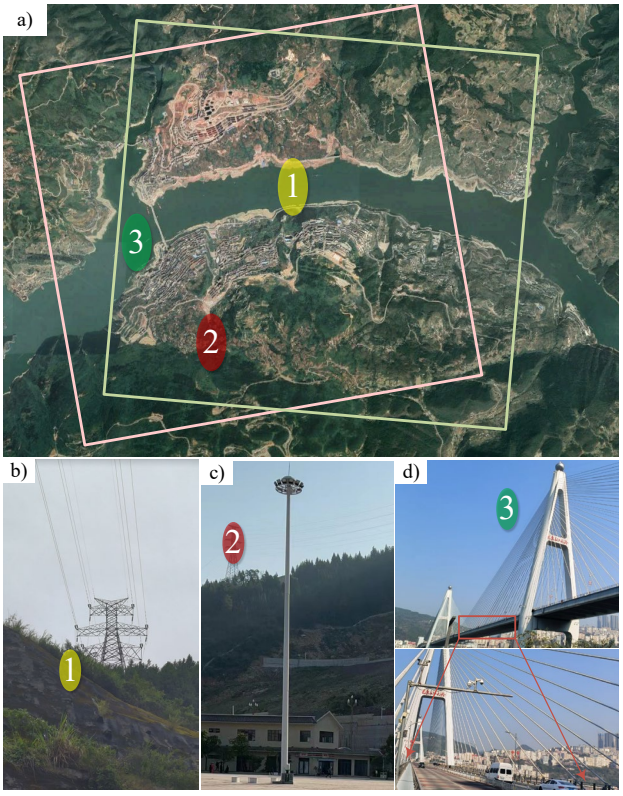

Figure 3. Three typical facilities in Badong. The TSX image coverage in (a). Study Area I site map in (b). Study Area II site map in (c). Study Area III site map in (d).

Study Area I is a cross-river power line within the Badong region, as shown in Figure 3b. The research area II is the Chayuan Square, which contains an independent light pole target in the middle of the square and ten light poles around the square in Figure 3c. The selected research area III is the Badong Yangtze River Bridge, which comprises complex structures forming the scattering patterns in SAR images. The typical planar features of the bridge's main interface and metal sphere target are chosen to discuss in Figure 3d.

In order to verify scattering point path tracking method, we have collected 54 ascending images and 48 descending TSX data images, with a difference in local incident angle of 8° and a time span of 2 years. Specific parameters are presented in Table 1.

orb	angle	Range	Azimuth	time	num
asc	37.7°	0.91m	1.26m	2019.12-2021.09	54
des	29.2°	0.91m	1.27m	2019.11-2021.09	48

Table 1. the parameter of TSX data obtained in Badong

2.3 LiDAR Cloud Points In Three Study Areas

The accurate 3D models of these artificial facilities are indispensable to validate the scattering point path tracking model. So, the liDAR cloud point data the three areas involving different typical targets were scanned using UVA.

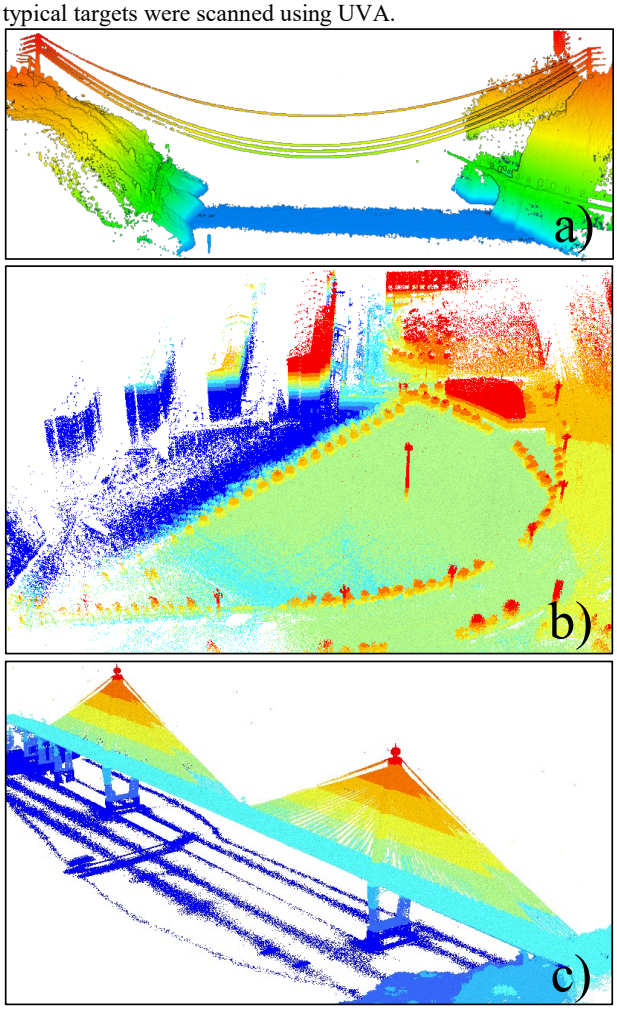

Figure 4 The LiDAR cloud point of the three Study Areas. Study Area I in (a). Study Area II in (b). Study Area III in (c).

Figure 4a shows the LiDAR point cloud in Study Area I, which consists of six transmission lines and two ground lines with a total length of 1220 meters and a direction of 17°. The diameter

of the power line is generally less than 5 cm, so the lines are considered as continuous point targets (Li Sha et al., 2014).
Figure 4b shows Study Area II, where is the Chayuan Square. The square is stable with an elevation of 397 meters. The middle light pole in the square have a height of 25 meters and have a thicker bottom and a thinner top. The lower cylindrical diameter is approximately 1.3 meters, while the upper cylindrical diameter is around 0.5 meters. The diameter of the poles is about 3.5 meters, forming a 12-sided column, as shown in Figure 3c.
Figure 4c shows Study Area III, which includes the Badong Yangtze River Bridge, a large bridge spanning the Yangtze River. The bridge has a total length of 900.6 meters and a main span of 388 meters. In this paper, the main structure of the Badong Bridge was divided into a metal sphere target and a surface structure on the main bridge deck for separate model analysis and simulation. The structure of the suspension cables is similar to power lines in Study Area I. While the radar signal reflection of the bridge deck is similar to the dihedral angle structure in Study Area II.

3. Results

3.1 Study Area I: Multi scattering features of power lines

The average intensity image of the TSX descending orbit data in Area I is shown in Figure 5a, where the water surface shows extremely low scattering intensity. As the distance increases, bright single scattering spots pointed out by the red arrow, less bright double scattering lines pointed by the green arrow, and faintly visible curved triple scattering features highlighted by the purple arrow can be seen. The scattering features of the same power line vary in multiple scattering imaging. There is clearly a range-oriented overlap in width for both double and triple scattering imaging due to the reflection surface involved in Area I with fluctuations of 30 meters annually. To better verify the scattering point path tracking method, 12 images from ascending orbit and 10 images from descending orbit, where the stable water level is at 174 meters, were selected to create an average intensity as a base map for overlaying the simulated results shown in Figure 5b~f.

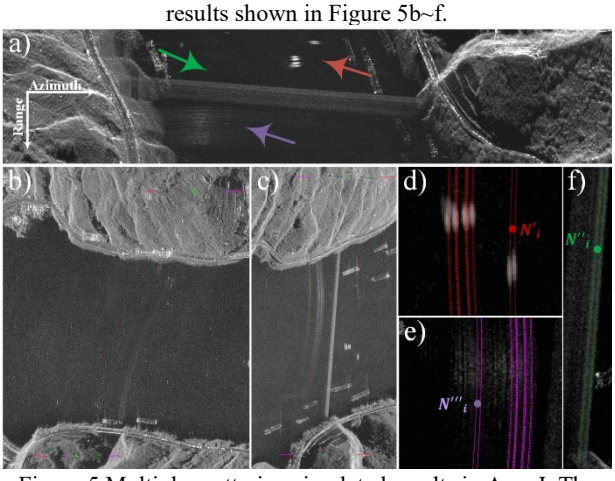

Figure 5 Multiple scattering simulated results in Area I. The SAR original average intensity in descending data. The red, green and purple arrow point to the imaging of multiple scattering respectively shown in (a). (b) and (c) show the average intensity in ascending and descending orbits at the same water level with simulation results superimposed. (d), (e), (f) are enlargements of the multiple scattering region in descending data.

Figure 5 shows the multiple scattering results of the power lines based on the proposed model, and the simulation results correspond well with the scattering results of the real SAR image. It also indicates that the multi-scattering features of power lines do not correspond to their real shape. Combined with the research (Yan et al., 2012), the single scattering feature of a total line forms an individual spot on SAR image. Moreover, the spot can only appear under strict geometric conditions. Specifically, when the angle between the direction of flight and the alignment of the power line is less than 15°. Thus, in Figure 5b, no obvious scattering features can be seen in ascending images for excessive angle. But we still find stable single scattering spots at the limit of the lines in every single SAR image. However, the double and triple scattering features are difficult to observe. It can be seen in the average image shown in Figure 6b that there is blurred double and triple scattering imaging on the water surface.
Figure 5c shows the descending results, indicating clearer multi-scattering features. The descending image shows the typical third scattering feature of power lines. To further verify the model, enlarged images of multiple scattering are shown in Figures 8d-f. The red simulated lines pass through the single scattering spots, and the double scattering features are consistent with the green simulated scattering line. For the triple bounce, the purple simulations also correspond to the triple scattering curves.
The single scattering spots are bright, while the double and triple scattering lines are weaker in intensity. In Figure 6d, the two narrow scattering spots of the lines on the right side correspond to the two ground wires, while on the left side, only four bright scattering spots are visible. The overlap of six power lines in the SAR image is indicated by the positions of the lines and the satellite parameters. The double scattering forms unstable straight scattering lines in real SAR data, while the triple scattering lines show as extremely weak curvatures. Also, there is a partially curved scattering feature in the average intensity, which is confirmed to be the triple scattering lines of the power lines based on the simulated results in this paper.
The validation above determined the multiple scattering characteristics of the power lines, particularly the imaging features of the triple scattering. It is important to note that the scattering characteristics of the power lines indicate the condition of the imaged section of the lines and do not directly represent the entire length. In addition, stable scattering features on the ground may be caused by special targets such as power lines or by multiple scattering.

3.2 Study Area II: Double scattering of light pole

Figure 6 is a schematic diagram showing the multiple scattering of light pole target. The red arrows represent the single bounce of the radar signal, while the green arrows represent the double bounce. The radar signal is reflected from the concrete surface and then reach the target, and finally returns to the satellite. The purple arrows represent the radar signal' triple bounce, which turns back in the same way when the reflected signal reaches the target. It should be noted that the dihedral angle structure formed by the light pole and the ground surface is very common in most artificial facilities, as shown in the dashed box in Figure 6. Double scattering occurs within this dihedral angle structure, resulting in a bright scattering spot in the SAR image. It is independent of the target's elevation according to Eq.3.
The square is unobstructed, providing a low scattering background in Figure 6a and d. The red points represent single scattering results, while the green and purple points represent the double and triple simulations, respectively. Figure 8b and Figure 8e are origin SAR images, where no single scattering features can be observed on the real SAR image. The side of the light pole forms a quite bright double scattering spot, regardless of the height of the elevation target. It is because that the radar signal in double bounce all normalised to the same pixel on SAR image.

The simulated double scattering results in green are coincide with the bright spots on the real SAR image in the two orbits shown in Figure 7a and d.

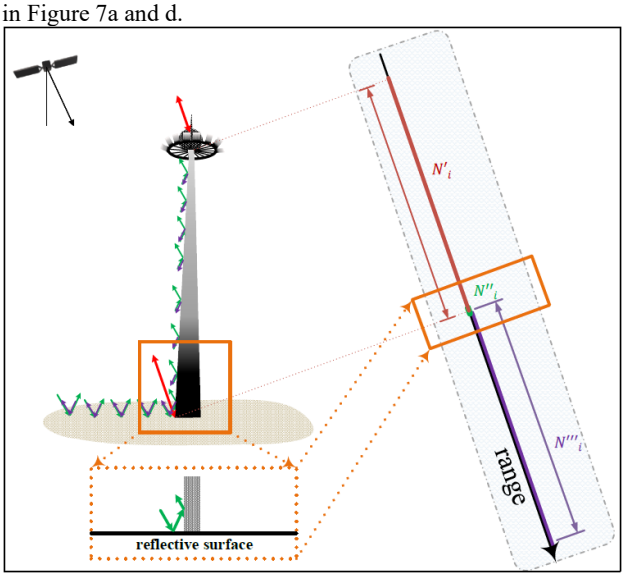

Figure 6 Multiple scattering model for light pole targets.

However, the intensity value of this double scattering spot differs significantly between ascending and descending images. The intensity value of the double scattering spot is approximately 76 dB in descending data while approximately 55 dB in ascending data. It may due to the different flight direction of the SAR sensor and the descending orbit aligns better consistency direction with the 12-sided shape of the poles. Thus, its edges have stronger double scattering, resulting in extremely high scattering intensity. At the same time, there are similar light poles around the square, which are similarly compressed to form bright double scattering points on the SAR image.

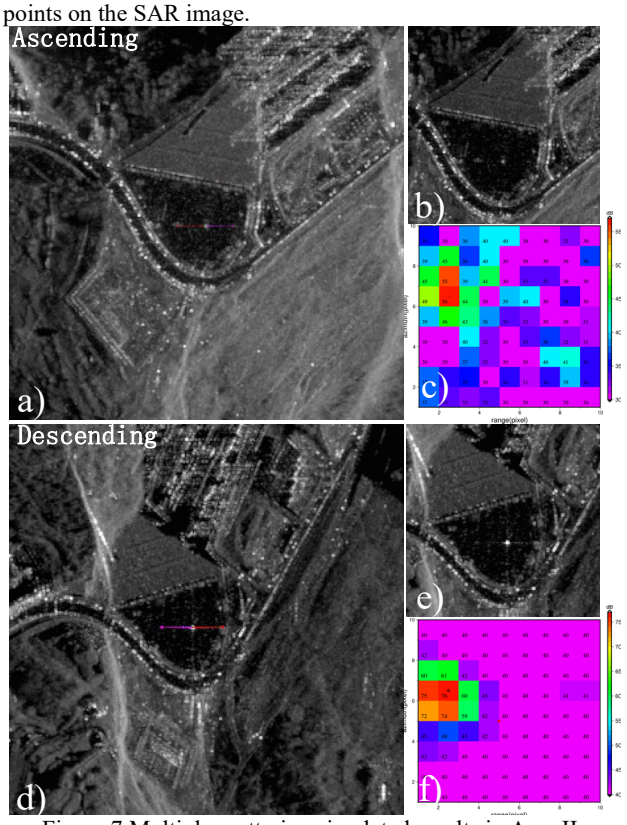

Figure 7 Multiple scattering simulated results in Area II. Ascending average intensity is (b), and (a) is the result of superimposing the simulated outcomes on (b). (c) is the intensity value of the light pole in ascending image. Descending average intensity is (d), and (e) is the result of superimposing the simulated outcomes on (d). (f) is the intensity value of the light pole in ascending image.

Importantly, the double scattering points formed by the light pole in both ascending and descending SAR images are good PS points. Moreover, the PS points can be observed in two orbits, which are good homonymous points that are well suited for the study of SAR imaging geodesy (Song et al., 2023), ground subsidence (Luo et al., 2014), deformation monitoring, and other related studies.

3.3 Study Area III: Complex Multi scattering of cable stayed bridge Targets

Figure 8 shows the schematic diagram of Badong Bridge and its multiple scattering, including the metal sphere and the main bridge deck. The red arrow indicates the single reflection of the radar signal, while the path illustrated by the green arrow indicates the process of the radar signal reaching the target via the reflective surface of the water surface and then returning to the satellite. The path illustrated by the purple arrows shows triple scattering, where the signal reaches the target via the reflective surface and then returns to the satellite following the original trajectory.

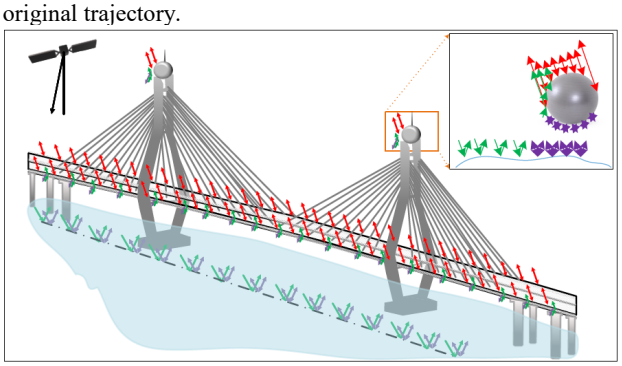

Figure 8 Multiple scattering model for point targets.

The target point N_i is derived from the LiDAR data, but the elevation of the reflecting surface N_{i_g} corresponding to N_i in the 48 descending and 54 ascending data is a varying quantity. The fluctuation of the Yangtze River water level within 145~175 meters is represented by the blue line in Figure 9a. In this paper, we chose the SAR images with an average value of water level between the period of 146 meters and 175 meters for the average intensity shown in Figure 9. Figure 9b and c indicate the simulated results in high level while Figure 9d and e shows the low-level results.

In Figure 9, the metal sphere at the top has a diameter of 6 meters and is visible in both orbits, occupying an area of 2*2 pixels. The multiple scattering features of radar signals are sequentially distributed in the range direction as N'_i, N''_i, N'''_i. Compared with the origin images without simulated results, the multiple scattering results are consistent with the real SAR image. The red features represent the single scattering, which shows the metal tip at the top, clearly reflecting the fine structure of the target body. The green features are the double scattering simulated results. And the locations of the green results also mark the locations of the double scattering on the main bridge deck. The double scattering results indicate that regardless of the shape of the target, it will be compressed into a small-pixels scattering feature in SAR images. The purple simulation results are not exactly agreement with the real SAR images. The triple scattering feature

appears as a blurred straight line in the azimuth direction, which indicates that energy loss and other situations may occur during the signal passes through the reflective surface.

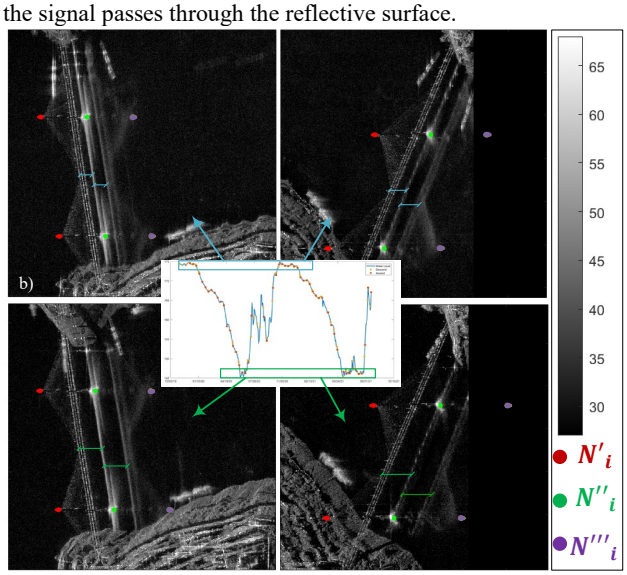

Figure 9 Simulated results of metal sphere in Area III. (a) Fluctuations in water levels in 2019-2021. (b) Average intensity in ascending data at high water level, with simulated results of the metal sphere. (c) Average intensity in descending data at high water level, with simulated results of the metal sphere. (d) Average intensity in ascending data at low water level, with simulated results of the metal sphere. (e) Average intensity in descending data at low water level, with simulated results of the metal sphere.

Multiple scattering extends the path only in the range direction and is very sensitive to the elevation changes of the reflecting surface. As the water level drops, the height difference between the target and the reflective surface continues to increase, which is reflected as an increase in range direction. If the water level rises, the pixel change in range is reversed. And the single and double scattering spots formed by the metal sphere are very clear at any water level. However, in current PSI algorithms, the PS points on the water surface are typically filtered out. So, it is worth exploring how to utilise these specific PS points for further study.

Figure 10 shows the multiple scattering simulations for the main bridge structures in both ascending and descending data. Figure 10b and Figure 10c show the average intensity image of the total data. The two figures indicate that the 30-meter water level fluctuation influence multiple scattering a lot. So, Figure 10a and Figure 10d display the average intensity base map at the same water level of 174 meters. The background is mostly the surface of the Yangtze River, making it easier to identify. In the 1 m resolution TSX images, the overall shape of the bridge can be clearly distinguished in both the ascending and descending images. The main bridge deck forms three distinct scattering lines in SAR. Except for the single scattering, which has similarities with the bridge structure, the double and triple scattering from the bridge are distributed sequentially as the range direction increases.

The bridge structures involved in single scattering are clearly visible. At the same time, a suspension structure participating in single scattering is also visible. Three separate scattering lines on SAR images represent the three reflective locations on the bridge surface. The double scattering lines, represented by green dotted lines, are visible. The horizontal bridge deck is compressed into small-pixels parallel to the azimuth, distributed parallel to the single scattering lines. The width of the double scattering lines depends on the height of the side deck, so theoretically, the double scattering lines are straight lines occupying a very small number of pixels. However, in ascending result, the double scattering lines are wider even at the same water level, which may be due to water surface fluctuations. The purple simulations represent the triple scattering results, and the features are blurred compared to the double and single scattering. And the triple one is the symmetry of single scattering about double scattering. The double scattering lines appear as brighter overlapping scattering lines in terms of intensity, whereas the triple scattering lines exhibit weaker energy loss for the radar signal.

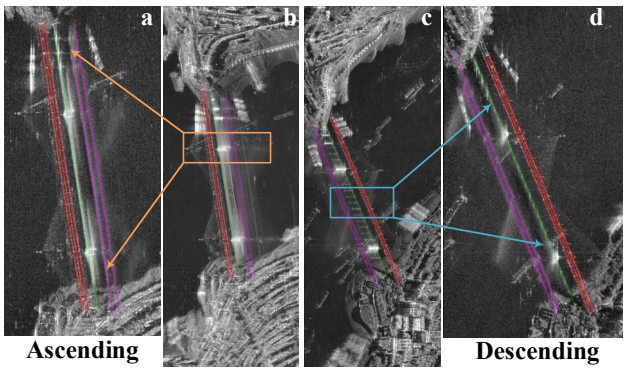

Figure 10 Simulated results of the main bridge structures in Area III. (a) Average intensity in ascending data at high water level, with simulated results of the main deck of the bridge. (b) Average intensity in ascending data of all images, with simulated results of the main deck of the bridge. (c) Average intensity in descending data of all images, with simulated results of the main deck of the bridge. (d) Average intensity in descending data at high water level, with simulated results of the main deck of the bridge.

In conclusion, the red, green, and purple simulations all correspond to the real SAR image, suggesting that the scattering point path tracking model performs well. The model can decode multiple scattering imaging under complex structures. But it should be noted that the bridge structure involved in the double scattering is not the main road surface of the bridge, but the side profile of the bridge deck. The location of the triple scattering is also different from the single and double ones, mainly involved in the substructure of the bridge. This suggests that the deformation calculated from the PS points of the bridge may consist of various structures in artificial facilities.

3.4 The impact of changing reflective surfaces on double and triple scattering

In long-term SAR images, it is difficult to ignore the change of the reflective surface. The reflective surface can cause a relatively large impact on multiple scattering imaging, which mainly consists of the roughness of the reflective surface (fluctuations of the water surface) and the change of the elevation of the reflecting surface (changes in the water level).

The reflecting surface in Study Area II is a concrete floor, so it is stable of roughness as well as elevation. And the double scattering formed by the streetlight is stable in average intensity. Whereas, the reflective surfaces in the other two Study Areas are water surfaces and there are 30-meters m water level variations as well as uncertain water surface fluctuations. Therefore, in average intensity, we can find the difference between the double and triple scattering features.

Figure 11 shows the multiple scattering features of power lines under different water level fluctuation in the descending dataset. Figure 11a displays the double scattering under 30-meters water

level fluctuations. The double scattering features occupies a line of considerable width in range direction. Figures 11b and 11c show the average intensity at high and low water level respectively. Figure 11d displays the double scattering, which is consistent with the double scattering and occupies more range-pixels at fluctuating water levels.

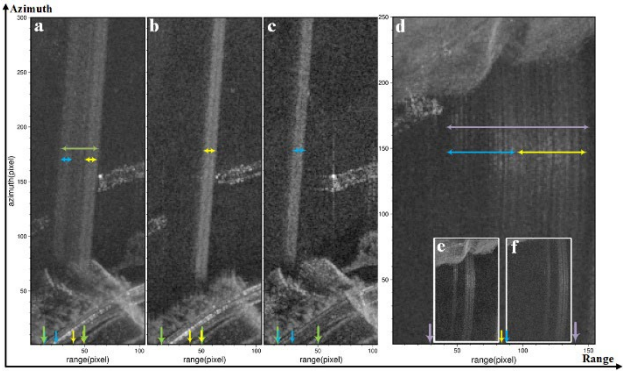

Figure 11 different water level in Area II. (a) Average intensity in descending data of all images, with the range of double scattering lines. (b) Average intensity in descending data at high water level, with the range of double scattering lines. (c) Average intensity in descending data at low water level, with the range of double scattering lines. (d) Average intensity in descending data of all images, with the range of triple scattering lines.

As for Bridge, 3.3 has shown detailed SAR images under different water levels. However, the double and triple scattering features still vary under the same water level. Thus, this section discusses the roughness of the reflective surface. Figure 12 displays the different condition of the water surface in average intensity. Figure 12a and Figure 12 d show the multiple scattering features under the static water surface. In this case, the single scattering area of the suspension cables and bridge decks can be clearly seen. With the fluctuation of the water level, double and triple scattering features occupy a certain range-pixel in the average intensity. Moreover, the double scattering features appear as points rather than lines both in ascending and descending orbit. Under this situation, the effects of different water level on double scattering features are only demonstrated in the range direction. It will be more obvious when comparing Figure 12a, b with Figure 12d and e.

In Figure 12b and Figure 12e, double scattering features occupy varying degrees of pixels in the azimuth direction including the suspension cables. And this is not due to the rise and fall of the water level, but probably due to the change in the reflective surface. Fluctuation of the water surface may result in a change in the reflective direction of the radar signal. So, we define that Figure 12b and 12e are under certain fluctuations on the water surface. Figure 12c shows there is a large area of interference in the water surface background, which is supposed to suffer the condition under larger waves. However, the single scattering lines can still be seen and the energy of double scattering may be further enhanced. It may due to signal scattering on multiple sides of the water waves. The triple scattering line is relatively blurred, but it can be distinguished as a symmetrical imaging feature, which also shows a certain width in range direction affected by the 30-meter water surface fluctuation.

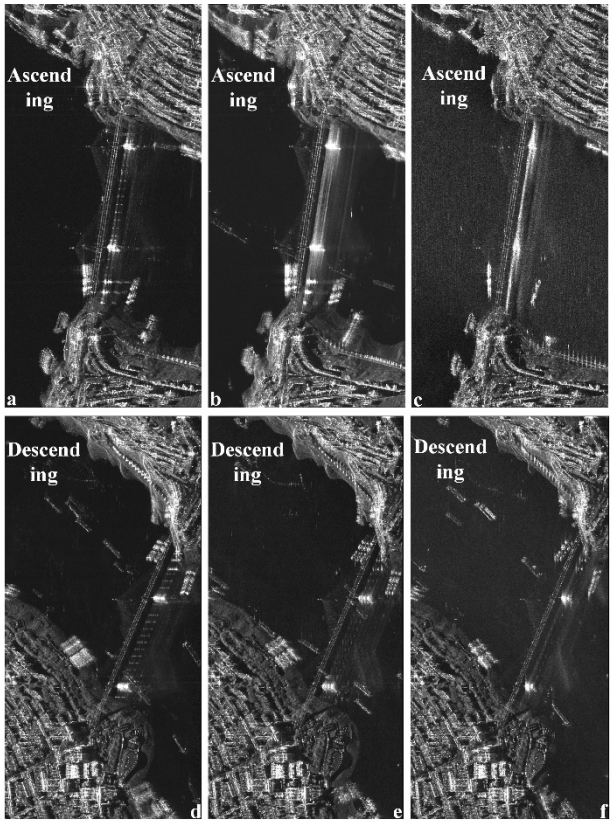

Figure 12 Ascending and descending SAR average intensity of different degrees of water surface in Area III. (a) Average intensity in ascending data under static water surface. (b) Average intensity in ascending data under a certain degree of water surface fluctuation. (c) Average intensity in ascending data under greater water surface fluctuations. (d) Average intensity in descending data under static water surface. (e) Average intensity in descending data under a certain degree of water surface fluctuation. (f) Average intensity in descending data under greater water surface fluctuations.

4. Conclusion

Large artificial targets exhibit unique multiple scattering features in high-resolution SAR images due to their distinctive geometric structure. Nevertheless, the extraction and analysis of the manufactured targets is challenging since these multiple scattering features frequently overlap with the background in SAR images. To profile the various scattering features in SAR images, we present a scattering point path tracking model in this study. TSX highlight datasets are used to test three Study Areas, comprising three typical artificial facilities, by utilizing their LiDAR cloud point data.

To directly validate, the simulated results have been positioned on average intensity SAR images. Firstly, simulated results agree well with the SAR multiple scattering features in range direction. The multiple scattering features only extend in range direction, which indicate that the proposed model is correct. And an accurate relationship with the local incident angle and the height of the reflective surface can be derived based on this model. Therefore, this model can be combined with larger real 3D data to confirm the targets’ location and then extract values from SAR images, such as elevation and deformation.

Subsequently, the scattering morphology of power lines in SAR images does not match the simulated results in Study Area I. It is vital to talk more about the power lines’ image on SAR data because it may have a relationship with the angle formed between

the targets' orientation and the radar flight direction. Thirdly, both ascending and descending datasets concurrently identify the double scattering spots created by the light poles in Study Area II. It is a useful and organic PS point for studies on ground subsidence, SAR imaging geodesy, deformation monitoring, and other related topics.

In addition, structures involved in multiple scattering are inconsistent under complex artificial facilities such as bridges. As a result, we need to stay mindful of the deformation values obtained by PS points, which may correspond to various facility sections. The resolution of SAR satellites is rapidly improving, therefore artificial facilities can no longer be simply viewed as completely formed. Rather, it needs to be oriented toward the refinement monitoring. Finally, we discovered that the multiple scattering of artificial facilities is significantly influenced by water's surface ripples after analysing the long time series of 102 images. Variations in water surface roughness and level have a significant impact on multiple scattering features.

In summary, the proposed scattering point path tracking model in this study is appropriate for multiple scattering in high resolution SAR images including powerlines, light poles, and bridges. The results provide a reference for the real target state of SAR image features and further providing an efficient new method for monitoring large artificial facility targets.

5. Acknowledgements

This work was sponsored by the National Natural Science Foundation of China (Nos. 42074031, 41674032, 41274048). The TSX data were provided by DLR under GEO1916.

6. References

Auer, S., Hinz, S., Bamler, R., 2010. Ray-Tracing Simulation Techniques for Understanding High-Resolution SAR Images. IEEE Trans. Geosci. Remote Sensing 48, 1445–1456. https://doi.org/10.1109/TGRS.2009.2029339

Bamler, R., Eineder, M., 2008. The Pyramids of Gizeh Seen by TerraSAR-X—A Prime Example for Unexpected Scattering Mechanisms in SAR. IEEE Geosci. Remote Sensing Lett. 5, 468–470. https://doi.org/10.1109/LGRS.2008.919378

Chen, Z., Li, T., Zhang, X., Li, S., Hou, A., Liu, Y., 2016. Long metal cable scattering features in space borne high resolution SAR images, in: 2016 IEEE International Geoscience and Remote Sensing Symposium (IGARSS). Presented at the 2016 IEEE International Geoscience and Remote Sensing Symposium (IGARSS), IEEE, Beijing, pp. 5982–5985. https://doi.org/10.1109/IGARSS.2016.7730563

Kim, S.-W., Lee, Y.-K., 2022. Accurate Water Level Measurement in the Bridge Using X-Band SAR. IEEE Geosci. Remote Sensing Lett. 19, 1–5. https://doi.org/10.1109/LGRS.2021.3138396

Lee, J.-S., Krogager, E., Ainsworth, T.L., Boerner, W.-M., 2006. Polarimetric Analysis of Radar Signature of a Manmade Structure. IEEE Geosci. Remote Sensing Lett. 3, 555–559. https://doi.org/10.1109/LGRS.2006.879564

Li Sha, Li Tao, Wang Mingzhou, Hou Ailing, Wu Wenhao, Xu Kan, Liu Yan, 2014. Study on extra-high voltage power line scatterers in time series SAR, in: 2014 Third International Workshop on Earth Observation and Remote Sensing Applications (EORSA). Presented at the 2014 3rd International Workshop on Earth Observation and Remote Sensing Applications (EORSA), IEEE, Changsha, China, pp. 47–51. https://doi.org/10.1109/EORSA.2014.6927847

Luo, Q., Perissin, D., Lin, H., Zhang, Y., Wang, W., 2014. Subsidence Monitoring of Tianjin Suburbs by TerraSAR-X Persistent Scatterers Interferometry. IEEE J. Sel. Top. Appl. Earth Observations Remote Sensing 7, 1642–1650. https://doi.org/10.1109/JSTARS.2013.2271501

Matikainen, L., Lehtomäki, M., Ahokas, E., Hyyppä, J., Karjalainen, M., Jaakkola, A., Kukko, A., Heinonen, T., 2016. Remote sensing methods for power line corridor surveys. ISPRS Journal of Photogrammetry and Remote Sensing 119, 10–31. https://doi.org/10.1016/j.isprsjprs.2016.04.011

Sarabandi, K., Moonsoo Park, 2003. A radar cross-section model for power lines at millimeter-wave frequencies. IEEE Trans. Antennas Propagat. 51, 2353–2360. https://doi.org/10.1109/TAP.2003.816380

Sarabandi, K., Moonsoo Park, 1999. Millimeter-wave radar phenomenology of power lines and a polarimetric detection algorithm. IEEE Trans. Antennas Propagat. 47, 1807–1813. https://doi.org/10.1109/8.817656

Sarabandi, K., Pierce, L., Oh, Y., Ulaby, F.T., 1994. Power lines: radar measurements and detection algorithm for polarimetric SAR images. IEEE Trans. Aerosp. Electron. Syst. 30, 632–643. https://doi.org/10.1109/7.272288

Shi, S., Hou, A., Liu, Y., Cheng, L., Chen, Z., 2021. SCATTERING CHARACTERISTICS OF ULTRA-HIGH-VOLTAGE POWER LINES IN SPACEBORNE SAR IMAGES. PIER M 102, 13–26. https://doi.org/10.2528/PIERM21020703

Shi, S., Liu, Y., Cheng, L., Chen, Z., 2020. Numerical Simulation of the Electromagnetic Scattering Characteristics of Ultra-High Voltage Power Line at X-Band, in: 2020 IEEE 6th International Conference on Computer and Communications (ICCC). Presented at the 2020 IEEE 6th International Conference on Computer and Communications (ICCC), IEEE, Chengdu, China, pp. 2289–2293. https://doi.org/10.1109/ICCC51575.2020.9345200

Soergel, U., Thiele, A., Gross, H., Thoennessen, U., 2007. Extraction of Bridge Features from high-resolution InSAR Data and optical Images, in: 2007 Urban Remote Sensing Joint Event. Presented at the 2007 Urban Remote Sensing Joint Event, IEEE, Paris, France, pp. 1–6. https://doi.org/10.1109/URS.2007.371882

Song, R., Wu, J., Song, X., Li, T., Zhang, L., 2023. 3-D Stereo Geolocation of Radar Reflectors Using Multiaspect SAR Acquisitions. IEEE Geoscience and Remote Sensing Letters 20, 1–5. https://doi.org/10.1109/LGRS.2023.3234546

Willetts, B., Stevens, M.B., Stove, A.G., Gashinova, M.S., 2018. Spectrum analysis of high-resolution SAR data to obtain Bragg signatures of power cables. IET Radar, Sonar & Navigation 12, 839–843. https://doi.org/10.1049/iet-rsn.2017.0574

Yan, L., Ailing, H., Sha, L., Xingkai, L., Tao, L., 2012. High Voltage Power Line Scattering Feature Analysis in Multi SAR Sensors and Dual Polarization. Second International Workshop on Earth Observation and Remote Sensing Applications.

Zeng, T., Gao, Q., Ding, Z., Tian, W., Yang, Y., Zhang, Z., 2017. Power Transmission Tower Detection Based on Polar Coordinate Semivariogram in High-Resolution SAR Image. IEEE Geosci. Remote Sensing Lett. 14, 2200–2204. https://doi.org/10.1109/LGRS.2017.2748819

Zhang, L., Liu, C., 2020. Oil Tank Extraction Based on Joint-Spatial Saliency Analysis for Multiple SAR Images. IEEE Geoscience and Remote Sensing Letters 17, 998–1002. https://doi.org/10.1109/LGRS.2019.2937355